

High-order photonic spin Hall effect and its application in high-contrast imaging

Shanshan He, Yichang Shou, Dingyu Xu[✉], Qiang Yang, Jiawei Liu, Shizhen Chen, and Hailu Luo^{✉*}
Laboratory for Spin Photonics, School of Physics and Electronics, Hunan University, Changsha 410082, China



(Received 25 September 2023; revised 3 January 2024; accepted 1 March 2024; published 21 March 2024)

The spin-orbit interaction of light has been extensively examined in reflection and refraction at diverse optical interfaces, which results in the discovery of photonic spin Hall effect (SHE). The fundamental physical essence of this effect is attributed to the one-order effect of polarization rotation associated with one-dimensional geometric phase gradient. Here, we report a unified frame of high-order photonic SHE, which is related to the two-order effect in spin-orbit interaction of light and two-dimensional geometric phase gradient. The conventional one-order photonic SHE is associated with the global transport of the wave vector in momentum space, while the high-order photonic SHE is attributed to the local transport. Direct experimental observation of high-order photonic SHE has been demonstrated in three conventional cases of focusing, diffraction, and scattering. Under the focusing and diffraction conditions, the edge-enhanced images based on the high-order photonic SHE can be realized by inserting two crossed polarizers into a nonparaxial optical system. Under the scattering condition, the confocal imaging system is introduced to observe the high-contrast image and motion trajectory of dynamic transparent particles. We believe that the high-order photonic SHE may develop promising image-processing technique and high-contrast microscopy.

DOI: 10.1103/PhysRevApplied.21.034045

I. INTRODUCTION

The spin-orbit interaction (SOI) of light is a striking effect in which the spin affects the spatial degrees of freedom of light, such as intensity distributions and propagation paths [1,2]. When linearly polarized light is reflected or refracted at a dielectric interface, the SOI leads to photons with opposite spin chirality moving in two opposite directions perpendicular to the refractive index gradient, and results in the observation of photonic spin Hall effect (SHE) [3,4]. The photonic SHE can be regarded as a direct optical analogy of the SHE in electronic systems where the electron spin and electric potential are replaced by the photon spin and refractive index gradient, respectively. The photonic SHE has been extensively investigated in reflection and refraction at diverse interfaces of optical materials, such as anisotropic crystal [5,6], topological insulators [7], metal film [8,9], semiconductors [10,11], metasurfaces [12–15], and two-dimensional atomic crystals [16–19]. In addition, spin-dependent shift or split of the beam intensity distribution arises, when a polarized beam of light is observed from a reference frame tilted with respect to the propagation direction. This effect has a purely geometric nature and amounts to and is referred to as geometric photonic SHE [20–25].

In general, the photonic SHE is a weak effect and the spin-dependent splitting is only a fraction of a

wavelength, therefore it cannot be detected directly by conventional optical measurements. By incorporating quantum weak measurements [26,27], however, the spin-dependent shift can be enhanced by nearly 4 orders of magnitude [28]. Based on weak-measurement technology, the spin-dependent shift acts as a pointer in the precise measurement of physical parameters, such as characterizing the parameters of nanostructures [8,29] and two-dimensional atomic crystals [30,31]. Moreover, the small spin-dependent splitting in photonic SHE enables optical spatial differential operations, which can be applied to edge detection and image processing [32–38]. The photonic SHE has potential applications in spin-controlled photonic devices and the emerging fields of spin photonics [39].

There are two motivations behind this work. First, inspired by the conventional photonic SHE at optical interfaces, we find that the tiny polarization-rotation effect in different optical systems share the same physics: parallel transport of polarization vectors in momentum space. Therefore, the polarization-rotation effect in focusing, diffraction, and scattering, can be simply explained as the result of high-order photonic SHE. Our theoretical model, although is not very rigorous, does not require complex diffraction integration in the calculation of the high-order polarization effect. It is shown that the conventional photonic SHE is attributed to the one-order effect of polarization rotation associated with one-dimensional geometric phase gradient. Here, the high-order photonic SHE arises from the two-order effect of polarization rotation, resulting

*hailuluo@hnu.edu.cn

in geometric phase gradients in two different dimensions. Second, we show that the output field in the imaging plane can be simply written as the second-order differentiation of the input field in different optical systems of focusing, diffraction, and scattering. Based on the high-order photonic SHE, we propose a compact two-dimensional optical spatial differentiator, which enables second-order differential operation using a pair of orthogonal polarizers. Further, we develop the application of high-order photonic SHE in high-contrast images of pure-phase objects. Based on the confocal microscope system, the high-contrast images and the trajectory of the dynamic transparent microspheres of biological cells are experimentally displayed.

II. HIGH-ORDER PHOTONIC SPIN HALL EFFECT

The SOI of light in diffraction, focusing, and scattering can be explained as the tiny polarization rotation of plane-wave components, which in order to satisfy the transversality of photon polarization [28,39]. The Hertz vector potential arises as a consequence of the transversality of the electromagnetic fields and Maxwell's equations [40,41]. Therefore, the Hertz vector potential should be introduced when establishing an intuitive physical picture of tiny polarization rotation. It is shown that the SOI of light depends on the geometry of the polarized vector evolution on momentum space, irrespective of either diffraction, focusing, or scattering. This is the reason why

these seemingly different field configurations, exhibit a correspondence in the theoretical frame.

The electric field $\tilde{\mathbf{E}}(\mathbf{k}, t)$ and the magnetic field $\tilde{\mathbf{B}}(\mathbf{k}, t)$ are determined by Maxwell's equations and can be written as $i\mathbf{k} \cdot \tilde{\mathbf{E}}(\mathbf{k}, t) = 0$, $i\mathbf{k} \cdot \tilde{\mathbf{B}}(\mathbf{k}, t) = 0$, $i\mathbf{k} \times \tilde{\mathbf{E}}(\mathbf{k}, t) + \partial \tilde{\mathbf{B}}(\mathbf{k}, t)/\partial t = 0$, and $i\mathbf{k} \times \tilde{\mathbf{B}}(\mathbf{k}, t) - 1/c^2 \partial \tilde{\mathbf{E}}(\mathbf{k}, t)/\partial t = 0$, where c is the speed of light in vacuum and $\mathbf{k} = k_x \mathbf{e}_x + k_y \mathbf{e}_y + k_z \mathbf{e}_z$ is the wave vector. The Hertz vector potential $\tilde{\Pi}(\mathbf{k}, t)$ needs to be introduced to describe electromagnetic wave propagation [42,43]:

$$\tilde{\mathbf{E}}(\mathbf{k}, t) = -\mathbf{k} \times [\mathbf{k} \times \tilde{\Pi}(\mathbf{k}, t)], \quad (1)$$

$$\tilde{\mathbf{B}}(\mathbf{k}, t) = \frac{1}{c^2} \left[i\mathbf{k} \times \frac{\partial \tilde{\Pi}(\mathbf{k}, t)}{\partial t} \right]. \quad (2)$$

Here, $\tilde{\Pi}(\mathbf{k}, t) = \mathbf{f}\tilde{\phi}(\mathbf{k}, t)/k^2$ can be written as the product of a constant vector and a scalar potential, which naturally arises as a consequence of the transversality of the electromagnetic fields (see Appendix A). The constant vector $\mathbf{f} = f_x \mathbf{e}_x + f_y \mathbf{e}_y$ is perpendicular to the propagation axis, which is determined by the input polarization. The scalar potential is determined by the initial input electric field $\tilde{\phi}(k_x, k_y) \propto \tilde{E}_{\text{in}}(k_x, k_y)$.

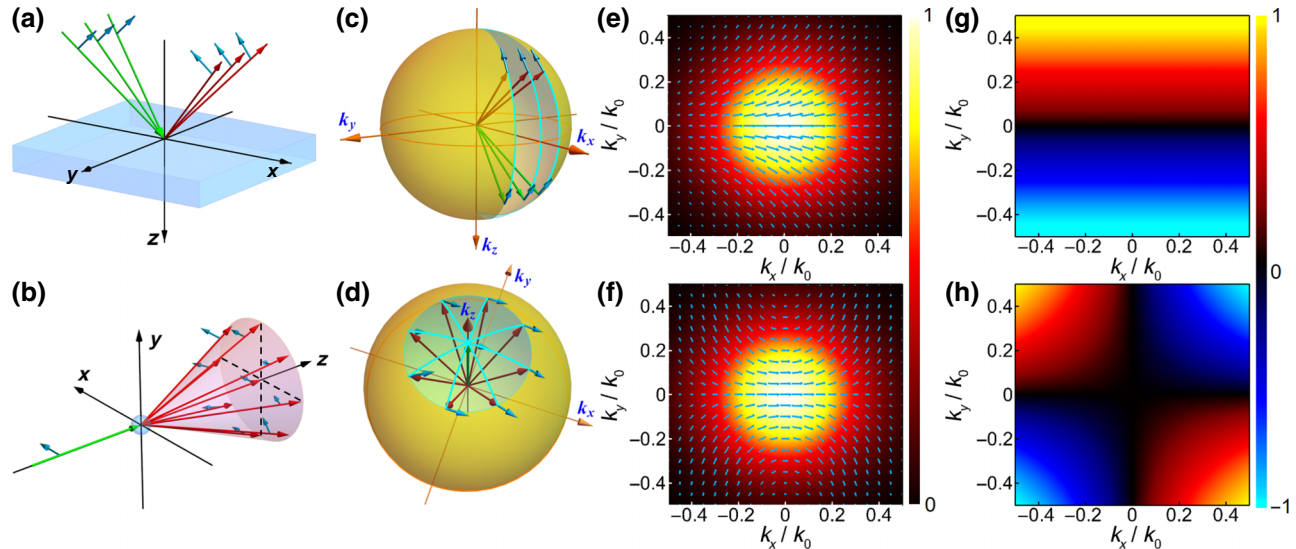


FIG. 1. An analogy between conventional photonic SHE and high-order photonic SHE. Green arrows represent incoming wave vectors, red arrows represent outgoing wave vectors, and blue arrows show linear polarization perpendicular to the wave vector. Tiny polarization rotation in (a) beam reflection at a dielectric interface and (b) beam scattering from a dielectric particle. (c),(d) show the parallel transport of polarization vectors in the momentum space corresponding to (a),(b), respectively. (e) Polarization distribution of the reflected light at a dielectric interface projected in the x - y plane. (f) Polarization distribution of the scattered light on a particle projected in the x - y plane. Here, we magnify this tiny polarization angle 100 times to make it easy to be observed. (g),(h) show the geometric phase distribution in (e),(f), respectively.

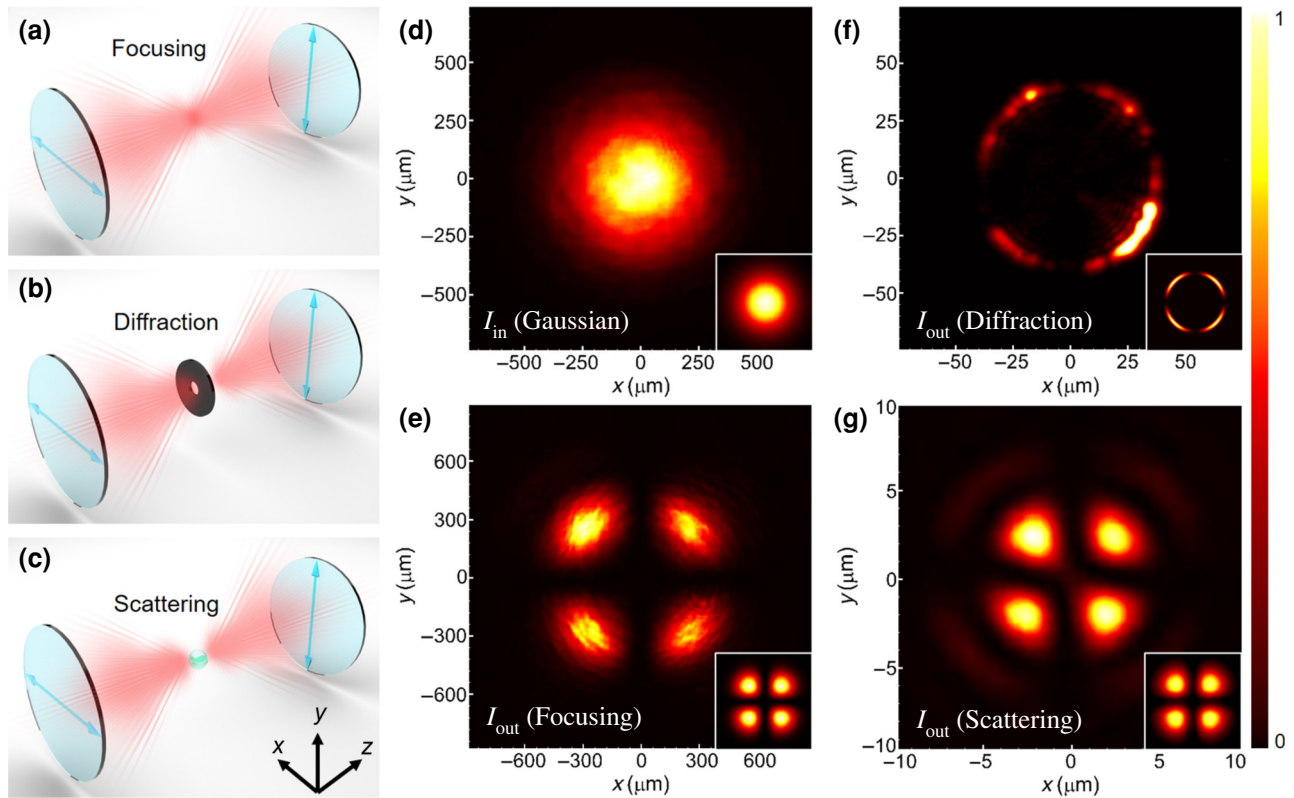


FIG. 2. High-order photonic SHE occurs in beam focusing, diffraction, and scattering. (a)–(c) show the experimental schematic diagrams: The arrows indicate the polarization direction of the polarizers. The diameter of aperture is chosen as 50 μm . The sphere indicates a 5- μm polystyrene microsphere. (d) The incident Gaussian linearly polarized light intensity comes from a He-Ne laser with a wavelength of 632.8 nm. The output light intensity through the crossed polarizers corresponds to (e) focusing, (f) aperture diffraction, and (g) particle scattering. Insets in (d)–(g) are corresponding theoretical results.

If we consider an input state of polarization with $\mathbf{f} = \mathbf{e}_x$, the electric field in momentum space becomes

$$\tilde{\mathbf{E}}(k_x, k_y) = \frac{1}{k^2} [(k^2 - k_x^2)\mathbf{e}_x + k_x k_y \mathbf{e}_y + k_x k_z \mathbf{e}_z] \tilde{E}_{in}(k_x, k_y). \quad (3)$$

It shows that the uniformly polarized beams will naturally undergo polarization changes during propagation, which is independent of light-matter interaction. With paraxial approximation, $k_x, k_y \ll k$, the dominant component of polarization in beam propagation is still the x direction.

The conventional one-order photonic SHE and high-order photonic SHE share the same physics: parallel transport of the polarization vector in momentum space. The one-order photonic SHE in reflection or refraction at optical interface is related to the global transport of the wave vector in momentum space, leading to the one-order polarization rotation ($\gamma \propto k_y/k$, where γ is the rotation angle) [3,4] [Figs. 1(a) and 1(c)]. However, the high-order photonic SHE is attributed to the local transport of the wave vector, resulting in two-order polarization rotation ($\gamma \propto k_x k_y/k^2$) on the momentum space [Figs. 1(b) and 1(d)]. In general, high-order photonic SHE is an extremely weak

optical effect, which is difficult to be found and easy to be ignored. When the beam is strongly focused or scattered, a second-order transverse electric field is induced under the nonparaxial condition.

We consider only polarization states in the x - y plane. The linear polarization consists of a circularly polarized substrate, satisfying $\mathbf{e}_x = (\mathbf{e}_+ + \mathbf{e}_-)/\sqrt{2}$ and $\mathbf{e}_y = i(\mathbf{e}_- - \mathbf{e}_+)/\sqrt{2}$, where \mathbf{e}_x represents the horizontal polarization and \mathbf{e}_y represents the vertical polarization. The polarization state of electric field is given by (see Appendix A)

$$\begin{aligned} \tilde{\mathbf{E}}(k_x, k_y) \approx & \frac{\tilde{E}_{in}(k_x, k_y)}{\sqrt{2}} \left[\exp\left(-i \frac{k_x k_y}{k^2}\right) \mathbf{e}_+ \right. \\ & \left. + \exp\left(+i \frac{k_x k_y}{k^2}\right) \mathbf{e}_- + \frac{k_x^2}{k^2} (\mathbf{e}_+ + \mathbf{e}_-) \right]. \end{aligned} \quad (4)$$

The SOI of light can be explained as the tiny polarization rotation of plane-wave components in order to satisfy the transversality of photon polarization [Figs. 1(e) and 1(f)]. The polarization rotation will induce a geometric phase gradient and ultimately lead to the spin-dependent shifts. In the conventional one-order photonic SHE, only one-dimensional geometric phase occurs as

shown in Fig. 1(g). In the high-order photonic SHE, however, two-dimensional phase gradient arises as shown in Fig. 1(h).

After passing through a polarizer whose polarization axis is parallel to the y axis, the output electric field in momentum space and position space can be, respectively, written as

$$\tilde{\mathbf{E}}_{\text{out}}(k_x, k_y) = \frac{k_x k_y}{k^2} \tilde{E}_{\text{in}}(k_x, k_y) \mathbf{e}_y, \quad (5)$$

$$\mathbf{E}_{\text{out}}(x, y) = -\frac{1}{k^2} \frac{\partial^2 E_{\text{in}}(x, y)}{\partial x \partial y} \mathbf{e}_y. \quad (6)$$

The detail derivation can be found in Appendix B. It is shown that the output field in the imaging plane can be simply written as the second-order differentiation of the input field. Therefore, a two-dimensional optical spatial differentiator can be produced based on the high-order photonic SHE.

III. HIGH-CONTRAST IMAGES

The schematic experimental setup and the output results of high-order photonic SHE in the beam focusing,

diffraction, and scattering are shown in Fig. 2. The beam vector propagates along the z axis. Because the high-order photonic SHE is a weak effect depended on nonparaxial wave-vector propagation, the large extinction ratio of the Glan linear polarizer make it difficult to observe in experiment. Particularly, we choose a plane polarizer (LPVISE100-A, Thorlabs) and 25-mm lens for experiments in Fig. 2(a). Diffraction and scattering situations in Figs. 2(b) and 2(c) naturally enhance the propagation of nonparaxial wave vectors and thus do not limit the type of polarizer. The diameter of small hole that produces diffraction is 50 μm , and the particle that produces scattering is a single polystyrene microsphere of 5 μm . Two polarizers with perpendicular polarization axes serve as preselected and postselected states. The camera beam quality analyzer (BC106N-VIS, Thorlabs) captures the outgoing light field. The preselected state controls the polarization of the incident light (the 632.8-nm Gaussian beam from He-Ne laser) along the horizontal direction, as shown in Fig. 2(d). Orthogonal postselected state produces a beam split in both the x and y directions, forming four spots shown in Figs. 2(e)–2(g). The experimental results correspond to the simulated polarization distribution. It proves to be consistent with the proposed physical model.

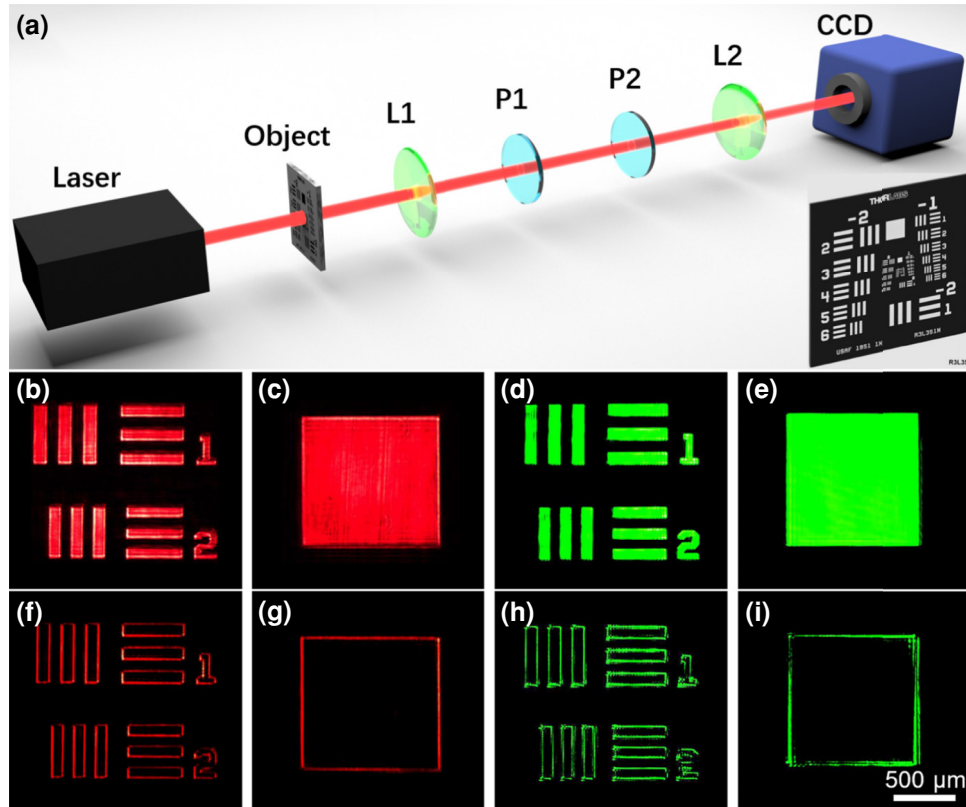


FIG. 3. High-contrast images of amplitude objects based on high-order photonic SHE. (a) Experimental setup for edge-enhanced imaging; light source is He-Ne laser (wavelength 632 nm); HWP, half-wave plate; P, polarizer (Economy Film Polarizer LPVISE100-A, Thorlabs); L, lens; CCD, charge-coupled device profiler measurement for laser beam. (b)–(e) are the bright-field images under laser illumination with wavelengths of 632.8 and 532 nm. (f)–(i) show the corresponding edge-enhanced images of (b)–(e), respectively.

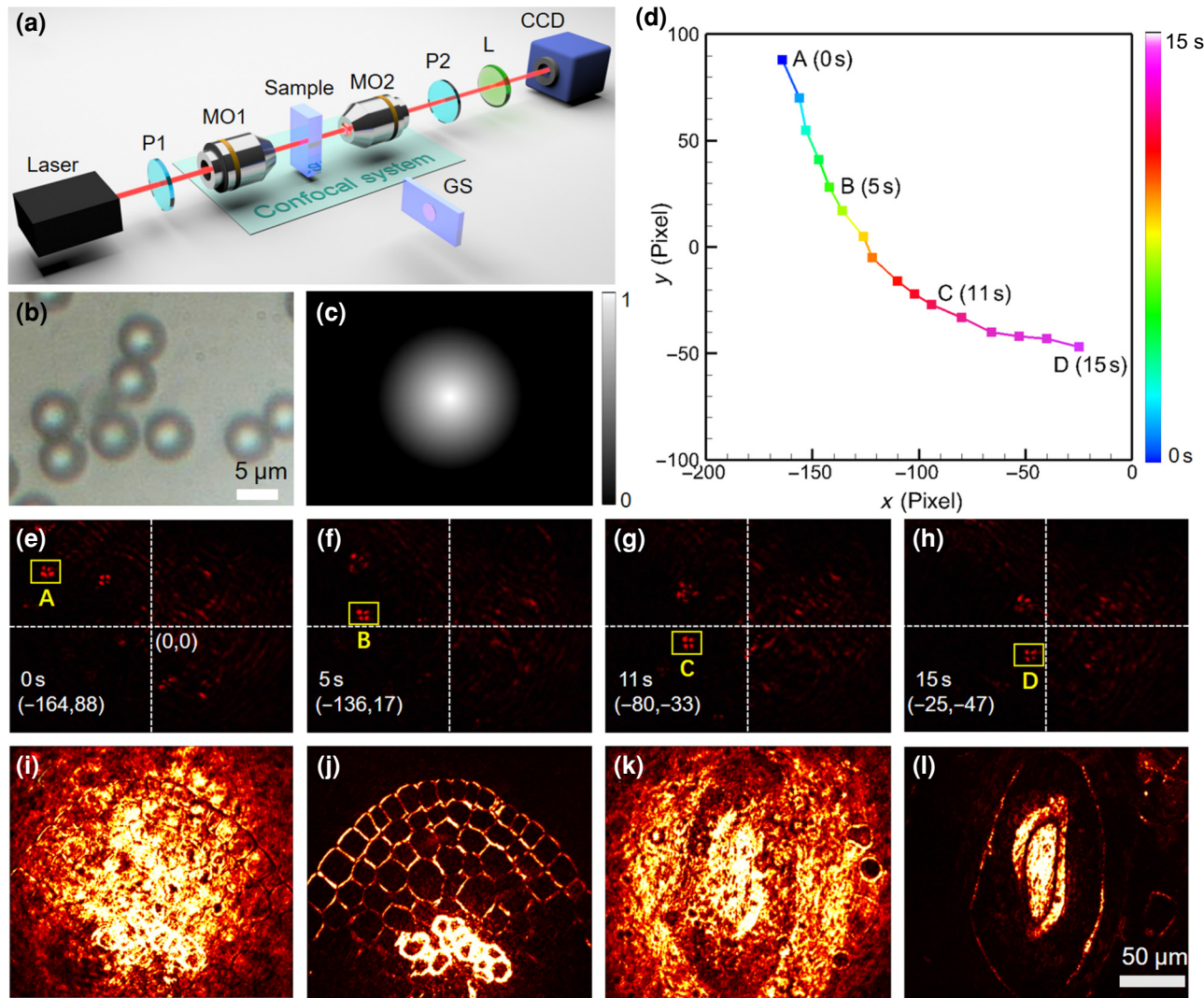


FIG. 4. Observation of high-contrast images of transparent samples based on high-order photonic SHE. (a) Schematic of the experimental setup. P, polarizer; MO, microscope objective. The numerical aperture (NA) of the objective $10\times$ and NA = 0.25. L, imaging lens; CCD, charge-coupled device; GS, glass slide. (b) The microscope image of polystyrene microspheres. Scale bars, 5 μm . (c) Phase distribution of a single transparent microsphere. (d) Trajectory of a polystyrene microsphere within 15 s. (e)–(h) High-contrast images of the observed microsphere, corresponding to the four different moments A to D marked in (d). (i),(j) are bright-field patterns and high-contrast images of broad bean leaf, respectively. (k),(l) are bright-field patterns and high-contrast images of hair follicle, respectively.

Unlike previously reported methods of edge detection, our proposed edge-imaging scheme based on the high-order photonic SHE effect can be realized by inserting two crossed polarizers into a nonparaxial optical system [Fig. 3(a)]. Figures 3(b)–3(e) show the complete bright-field images when the two polarizers are parallel to each other. The amplitude target, corresponding to the light-intensity distribution pattern (USAF-1951, Thorlabs), is placed at the front focal plane of the first lens (L1), and the CCD is placed at the back focal plane of the second lens. Both P1 and P2 do not have to be placed at the focal point of the lens. The function of P1 is to provide the

initial horizontally polarized beam, and placing it before or after L1 will not affect the differential operation. The role of L1 is to establish nonparaxial conditions, and L2 is the lens used for imaging. When only the two polarizers are crossed, edge-enhanced images of different objects are obtained [Figs. 3(f)–3(i)]. In order to prove that the performance of the differentiator is not affected by the wavelength, the light source is set to lasers with two wavelengths ($\lambda = 632.8 \text{ nm}$ and $\lambda = 532 \text{ nm}$). In the imaging experiments, edge images at different wavelengths can also be obtained. This shows that the transmission efficiency of the differentiator based on the high-order photonic SHE

can support the conventional CCD to acquire edge images under orthogonal conditions, and has good performance in the field of image processing.

Figure 4 shows the experimental setup and results of dynamic particles and two cell slices. The polarizer and light source of Fig. 4(a) are the same as in Fig. 3(a). Monodisperse polystyrene plastic microspheres of 5 μm in pure water are used as the observed sample packed in a 5-mm-wide quartz cuvette. The microscope image and phase distribution of individual microsphere are shown in Figs. 4(b) and 4(c). We set the center point of the CCD screen as the coordinate origin, and set the focal length of the confocal microscope system to 0 s until a microsphere is clearly located. The observation ends when the microsphere moves out of focus. Figure 4(d) is the trajectories of a polystyrene microsphere in the certain x - y plane. Figures 4(e)–4(h) are images of individual microspheres corresponding to the four different time points in Fig. 4(d). We choose broad bean leaf and human skin hair follicle as observation samples. By adjusting the two polarizers in parallel or orthogonal condition, we observe bright- and dark-field images as shown in Figs. 4(i)–4(l). Compared to the bright-field microscopy images, crossed polarizers result in dark-field performance, eliminating background noise and interference from other samples that are not in the focal plane. Therefore, high-order photonic SHE enables high-contrast imaging of dynamically transparent microspheres and cells.

Clover-shaped intensity distributions are widely found in different optical systems, such as crossed polarizers, particle scattering, and strong focusing [44–46]. To explain these unusual optical phenomena, a variety of different propagation models (oblique incidence and nonparaxial conditions) [47,48], scattering theory involving complex integration operations [49], and high numerical aperture optical microscopy with strong SOI have been proposed. The SOI of light on focusing by a high-numerical-aperture lens or scattering a small particle has also been extensively studied [50–53]. Here, the SOI of light in different imaging systems are described as high-order photonic SHE. Furthermore, the output field in the imaging plane can be expressed as the second-order differentiation of the input field in the object plane. It should be noted that the differentiation relationship no longer holds at other transmission distances.

IV. CONCLUSION

In conclusion, the high-order photonic SHE has been proposed based on the second-order solution of Maxwell's equations. This effect can be described as the two-dimensional displacement of the components with opposite spins during the propagation process of light-matter interaction. Under the orthogonal postselection setting, the transverse output electric field produces two-dimensional

splitting to form light spots distributed in four quadrants. Its physical principle is explained as tiny polarization rotation due to the transversality of photon polarization during the parallel transport of polarization vector in the momentum space. Our scheme, although is not very rigorous, does not require complex diffraction integration in the calculation of the high-order polarization effect. The one-order photonic SHE and high-order photonic SHE share the same physics: Parallel transport of the polarization vector in momentum space. The local transport of polarization vectors would result in two-dimensional geometric phase gradient, and eventually lead to the high-order photonic SHE. These results may provide a deeper understanding of SOI of light. In addition, the orthogonal postselection filters out the low wave vector and allows the high one to pass, which works as a high-pass filter. Therefore, the high-order photonic SHE may also be combined with imaging systems to develop spatial differentiation operations and all-optical image processing techniques. In the light-scattering system, the high-contrast images of individual microspheres are obtained, which provide possible applications in visualization of transparent particles.

ACKNOWLEDGMENTS

This work was supported by National Natural Science Foundation of China (Grant No. 12174097), the Natural Science Foundation of Hunan Province (Grant No. 2021JJ10008).

APPENDIX A: THEORETICAL MODEL OF HIGH-ORDER PHOTONIC SHE

For a rigorous description of electromagnetic wave propagation, the Hertz vector potential $\tilde{\Pi}(\mathbf{k}, t)$ is an exact solution of the Helmholtz wave equation:

$$\nabla^2 \tilde{\Pi}(\mathbf{k}, t) - \frac{1}{c^2} \frac{\partial^2 \tilde{\Pi}(\mathbf{k}, t)}{\partial t^2} = 0. \quad (\text{A1})$$

Here, $\tilde{\Pi}(\mathbf{k}, t) = \mathbf{f}\tilde{\phi}(\mathbf{k}, t)/k^2$ can be written as the product of a constant vector and a scalar field. The scalar field cannot represent an electromagnetic wave because both the electric and magnetic field are vector field. This problem can be overcome by associating with a constant unit vector \mathbf{f} . Furthermore, the scalar and vector potentials are defined as [54,55]

$$\tilde{\Phi}(\mathbf{k}, t) = -\nabla \cdot \tilde{\Pi}(\mathbf{k}, t), \quad (\text{A2})$$

$$\tilde{A}(\mathbf{k}, t) = \frac{\partial \tilde{\Pi}(\mathbf{k}, t)}{\partial t}. \quad (\text{A3})$$

The electric and magnetic fields are then obtained as

$$\tilde{\mathbf{E}}(\mathbf{k}, t) = -\nabla \tilde{\Phi}(\mathbf{k}, t) - \frac{\partial \tilde{\mathbf{A}}(\mathbf{k}, t)}{\partial t}, \quad (\text{A4})$$

$$\tilde{\mathbf{B}}(\mathbf{k}, t) = \nabla \times \tilde{\mathbf{A}}(\mathbf{k}, t). \quad (\text{A5})$$

After substituting Eqs. (A2) and (A3) into Eqs. (A4) and (A5), we get

$$\tilde{\mathbf{E}}(\mathbf{k}, t) = -\mathbf{k} \times [\mathbf{k} \times \tilde{\Pi}(\mathbf{k}, t)], \quad (\text{A6})$$

$$\tilde{\mathbf{B}}(\mathbf{k}, t) = \frac{1}{c^2} \left[i\mathbf{k} \times \frac{\partial \tilde{\Pi}(\mathbf{k}, t)}{\partial t} \right]. \quad (\text{A7})$$

When the arbitrary linearly polarized beam propagates along the z axis, $\mathbf{f} = \cos \alpha \mathbf{e}_x + \sin \alpha \mathbf{e}_y$, where α is the angle between the incident polarization direction and the x axis. The Hertz vector becomes $\tilde{\Pi}(\mathbf{k}, t) = (\cos \alpha \mathbf{e}_x + \sin \alpha \mathbf{e}_y)\tilde{\phi}(\mathbf{k}, t)/k^2$. From Eq. (1), the electric field can be written as

$$\begin{aligned} \tilde{\mathbf{E}}(k_x, k_y) &= \frac{\tilde{E}_{\text{in}}(k_x, k_y)}{k^2} \left[(k_x^2 \cos \alpha + k_x k_y \sin \alpha + k^2 \cos \alpha) \mathbf{e}_x \right. \\ &\quad + (k_x k_y \cos \alpha + k_y^2 \sin \alpha + k^2 \sin \alpha) \mathbf{e}_y \\ &\quad \left. + (k_x k_z \cos \alpha + k_y k_z \sin \alpha) \mathbf{e}_z \right]. \end{aligned} \quad (\text{A8})$$

We consider only polarization states in the x - y plane. The electric field can be expressed in spin basis: $\mathbf{e}_x = (\mathbf{e}_+ + \mathbf{e}_-) / \sqrt{2}$ and $\mathbf{e}_y = i(\mathbf{e}_- - \mathbf{e}_+) / \sqrt{2}$. Equation (A8) can be rewritten as

$$\begin{aligned} \mathbf{E}(k_x, k_y) &= \frac{\tilde{E}_{\text{in}}(k_x, k_y)}{\sqrt{2}k^2} \left[k_x^2 \cos \alpha + k_x k_y \sin \alpha + k^2 \cos \alpha \right. \\ &\quad - i(k_x k_y \cos \alpha + k_y^2 \sin \alpha + k^2 \sin \alpha) \mathbf{e}_+ \\ &\quad + \frac{\tilde{E}_{\text{in}}(k_x, k_y)}{\sqrt{2}k^2} \left[k_x^2 \cos \alpha + k_x k_y \sin \alpha + k^2 \cos \alpha \right. \\ &\quad \left. + i(k_x k_y \cos \alpha + k_y^2 \sin \alpha + k^2 \sin \alpha) \mathbf{e}_- \right]. \end{aligned} \quad (\text{A9})$$

When we choose $\alpha = 0$, the polarization state of electric field is given by

$$\begin{aligned} \mathbf{E}(k_x, k_y) &= \frac{\tilde{E}_{\text{in}}(k_x, k_y)}{\sqrt{2}k^2} [(k_x^2 + k^2 - ik_x k_y) \mathbf{e}_+ \\ &\quad + (k_x^2 + k^2 + ik_x k_y) \mathbf{e}_-]. \end{aligned} \quad (\text{A10})$$

After introducing the approximation: $1 + ik_x k_y \approx \exp(+ik_x k_y)$, we get

$$\begin{aligned} \mathbf{E}(k_x, k_y) &\approx \frac{\tilde{E}_{\text{in}}(k_x, k_y)}{\sqrt{2}} \left[\exp\left(-i \frac{k_x k_y}{k^2}\right) \mathbf{e}_+ \right. \\ &\quad \left. + \exp\left(+i \frac{k_x k_y}{k^2}\right) \mathbf{e}_- + \frac{k_x^2}{k^2} (\mathbf{e}_+ + \mathbf{e}_-) \right]. \end{aligned} \quad (\text{A11})$$

The first term is in the same direction as the input linear polarization. The terms of $\exp(-ik_x k_y/k^2) \mathbf{e}_+$ and $\exp(+ik_x k_y/k^2) \mathbf{e}_-$ present two-dimensional opposite phase gradients in the x and y directions. The polarization rotation will induce a geometric phase gradient and ultimately lead to the spin-dependent shifts. When the polarization rotation occurs in momentum space, the spatial shift will be induced in position space.

The polarization rotation can be explained as the origin of photonic SHE. In general, an arbitrary linear polarization state can be decomposed into two orthogonally circular polarization states with opposite phases:

$$\begin{pmatrix} \cos \gamma \\ \sin \gamma \end{pmatrix} = \exp(-i\varphi_G) |+\rangle + \exp(+i\varphi_G) |-\rangle, \quad (\text{A12})$$

where γ is the polarization angle. The tiny polarization rotation will induce a geometric phase gradient and ultimately lead to the spin-dependent shifts. In conventional one-order photonic SHE, the polarization rotation is related to one-dimensional geometric phase $\varphi_G \propto k_y/k$. The polarization rotation occurs in momentum space, the spatial shift will be induced $\sigma \partial \varphi_G / \partial k_y$. In the two-order photonic SHE, the polarization rotation is related to two-dimensional geometric phase $\varphi_G \propto k_x k_y / k^2$.

APPENDIX B: OPTICAL DIFFERENTIATION AND IMAGE EDGE DETECTION

After the beam passing through second polarizer whose polarization axis is chosen as $\beta = \alpha + \pi/2$, and the Jones matrix can be written as

$$J = \begin{bmatrix} \cos^2 \beta & \sin \beta \cos \beta \\ \sin \beta \cos \beta & \sin^2 \beta \end{bmatrix}. \quad (\text{B1})$$

The final electrical field in momentum space through crossed polarizers can be written as

$$\begin{aligned}\tilde{\mathbf{E}}_{\text{out}}(k_x, k_y) &= \frac{\tilde{E}_{\text{in}}(k_x, k_y)}{k^2} \times J \times \left[\begin{array}{c} k_x^2 \cos \alpha + k_x k_y \sin \alpha + k^2 \cos \alpha \\ k_x k_y \cos \alpha + k_y^2 \sin \alpha + k^2 \sin \alpha \end{array} \right] \\ &= \frac{\tilde{E}_{\text{in}}(k_x, k_y)}{k^2} \times \left[\begin{array}{c} \sin \alpha \left[-k_x k_y \cos 2\alpha + (k_x^2 - k_y^2) \cos \alpha \sin \alpha \right] \\ \cos \alpha \left[k_x k_y \cos 2\alpha + (k_y^2 - k_x^2) \cos \alpha \sin \alpha \right] \end{array} \right].\end{aligned}\quad (\text{B2})$$

When $\alpha = 0$, the output field in the imaging plane can be written as

$$\tilde{\mathbf{E}}_{\text{out}}(k_x, k_y) = \frac{\tilde{E}_{\text{in}}(k_x, k_y)}{k^2} \begin{bmatrix} 0 \\ k_x k_y \end{bmatrix}. \quad (\text{B3})$$

The field in the real (position) space can be obtained using the inverse Fourier transform:

$$\mathbf{E}_{\text{in}}(x, y) = \int \int \tilde{E}_{\text{in}}(k_x, k_y) \exp(ik_x x + ik_y y) dk_x dk_y. \quad (\text{B4})$$

After the two-order differential operation, Eq. (B4) can be written as

$$\begin{aligned}\frac{\partial^2 E_{\text{in}}(x, y)}{\partial x \partial y} &= - \int \int k_x k_y \tilde{E}_{\text{in}}(k_x, k_y) \\ &\quad \exp(ik_x x + ik_y y) dk_x dk_y.\end{aligned}\quad (\text{B5})$$

The output electric field in the position space is

$$\mathbf{E}_{\text{out}}(x, y) = -\frac{1}{k^2} \frac{\partial^2 E_{\text{in}}(x, y)}{\partial x \partial y} \mathbf{e}_y. \quad (\text{B6})$$

Similarly, when $\alpha = \pi/2$, the output field can be obtained as

$$\tilde{\mathbf{E}}_{\text{out}} = \frac{\tilde{E}_{\text{in}}(k_x, k_y)}{k^2} \begin{bmatrix} k_x k_y \\ 0 \end{bmatrix}. \quad (\text{B7})$$

The output electric field in the position space is given by

$$\mathbf{E}_{\text{out}}(x, y) = -\frac{1}{k^2} \frac{\partial^2 E_{\text{in}}(x, y)}{\partial x \partial y} \mathbf{e}_x. \quad (\text{B8})$$

The spatial transform between the input and output electric fields is determined by a spatial spectral transfer function:

$$H(k_x, k_y) = \tilde{E}_{\text{out}}(k_x, k_y) / \tilde{E}_{\text{in}}(k_x, k_y) \propto k_x k_y. \quad (\text{B9})$$

Notably, the two-dimensional optical differentiator with isotropic transfer function $H(k_x, k_y) = C_x k_x + C_y k_y$ ($C_y/C_x = \pm i$) has been proposed [56]. Isotropic edge

detection means that the complete edges of images are displayed with the same intensity. Here, the transfer function $H(k_x, k_y) \propto k_x k_y$ of the high-order photonic SHE differentiator is anisotropic but does not affect two-dimensional edge detection. As shown in Fig. 3(g), the edge information of the four edges of the square pattern is complete. In addition, the high-order photonic SHE is dependent on nonparaxial wave-vector propagation, which implies a large spatial bandwidth for the differentiator, but the tiny k_x and k_y components also pose some difficulties for experimental observation. Meanwhile, the optical components for realizing the high-order photonic SHE is fewer and simpler to operate. Based on the high-order photonic SHE, we propose a compact, low cost, and two-dimensional optical spatial differentiator, which enables second-order differential operation and edge imaging using a pair of orthogonal polarizers.

It is rather counterintuitive, since two crossed polarizers cannot transmit a beam. Therefore, we must first establish the nonparaxial condition, which is reflected in increasing the wave-vector components k_x and k_y of the beam. Then, the transfer function is measured experimentally and the spatial differentiation operation of the differentiator is verified. The experimental setup is shown in Fig. 5, the light source is a 632.8-nm He-Ne laser. The polarizer (P) is a thin plate with a dichroic film. P1 and P2 do not need to be in focus between the two lenses. It is worth noting that the Glan laser polarizer is not suitable for this experiment due to its unique structure. The combination of lenses L1 and L2 constitutes a $4f$ system with $f = 25$ mm [Figs. 5(b)–5(d)] and $f = 100$ mm [Figs. 5(e)–5(g)]. The CCD is a laser beam profiler that records the two-dimensional density distribution of the beam power. When the polarization axes of the two polarizers are arranged parallel, the CCD captures the initial incident Gaussian field. If the polarization axis of the second polarizer is adjusted perpendicular to that of the first polarizer, the output light field similar to the second-order Hermite-Gaussian mode is obtained. Experimental measurements of the transfer function are obtained by processing the data extracted from the initial and output light fields [Figs. 5(d) and 5(g)]. We compare two different nonparaxial conditions: the role of L1 is to provide different k_x and k_y components. This proves that the stronger the focusing ability, the larger the k_x and k_y components of the beam, and the more obvious the high-order photonic SHE.

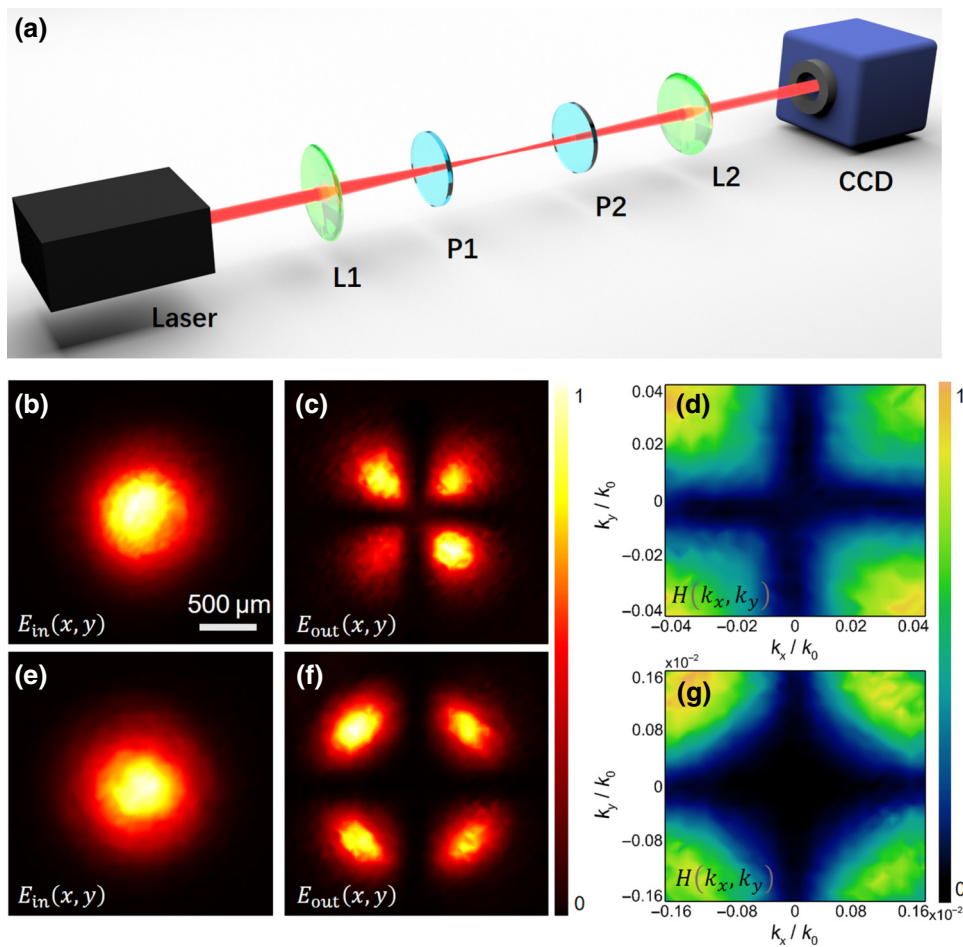


FIG. 5. Two-dimensional optical transfer function measured experimentally under the two lenses with different focal lengths. (a) Diagram of the experimental setup, the light source is He-Ne laser (wavelength 632.8 nm); P, polarizer (Economy Film Polarizer LPVISE100-A, Thorlabs); L, lens; CCD, used for the measurement of the charge-coupled device profiler of the laser beam. (b)–(d) The input and output optical field intensity and the transfer function of the differentiator under the condition of a 25-mm lens. (e)–(g) The input and output optical field intensity and the transfer function of the differentiator under the condition of a 100-mm lens.

- [1] K. Y. Bliokh, F. J. Rodríguez-Fortuño, and F. Nori, Spin-orbit interactions of light, *Nat. Photon.* **9**, 796 (2015).
- [2] X. Ling, X. Zhou, K. Huang, Y. Liu, C.-W. Qiu, H. Luo, and S. Wen, Recent advances in the spin Hall effect of light, *Rep. Prog. Phys.* **80**, 066401 (2017).
- [3] M. Onoda, S. Murakami, and N. Nagaosa, Hall effect of light, *Phys. Rev. Lett.* **93**, 083901 (2004).
- [4] K. Y. Bliokh and Y. P. Bliokh, Conservation of angular momentum, transverse shift, and spin Hall effect in reflection and refraction of an electromagnetic wave packet, *Phys. Rev. Lett.* **96**, 073903 (2006).
- [5] K. Y. Bliokh, C. T. Samlan, C. Prajapati, G. Puentes, N. K. Viswanathan, and F. Nori, Spin-Hall effect and circular birefringence of a uniaxial crystal plate, *Optica* **3**, 1039 (2016).
- [6] W. Zhu, H. Zheng, Y. Zhong, J. Yu, and Z. Chen, Wavevector-varying Pancharatnam-Berry phase photonic spin Hall effect, *Phys. Rev. Lett.* **126**, 083901 (2021).

- [7] X. Zhou, J. Zhang, X. Ling, S. Chen, H. Luo, and S. Wen, Photonic spin Hall effect in topological insulators, *Phys. Rev. A* **88**, 053840 (2013).
- [8] X. Zhou, Z. Xiao, H. Luo, and S. Wen, Experimental observation of the spin Hall effect of light on a nanometal film via weak measurements, *Phys. Rev. A* **85**, 043809 (2012).
- [9] J. Ren, Y. Li, Y. Lin, Y. Qin, R. Wu, J. Yang, Y. F. Xiao, H. Yang, and Q. Gong, Spin Hall effect of light reflected from a magnetic thin film, *Appl. Phys. Lett.* **101**, 171103 (2012).
- [10] J.-M. Ménard, A. E. Mattacchione, M. Betz, and H. M. van Driel, Imaging the spin Hall effect of light inside semiconductors via absorption, *Opt. Lett.* **34**, 2312 (2009).
- [11] J.-M. Ménard, A. E. Mattacchione, H. M. Driel, C. Hautmann, and M. Betz, Ultrafast optical imaging of the spin Hall effect of light in semiconductors, *Phys. Rev. B* **82**, 045303 (2010).
- [12] X. Yin, Z. Ye, J. Rho, Y. Wang, and X. Zhang, Photonic spin Hall effect at metasurfaces, *Science* **339**, 1405 (2013).

- [13] N. Shitrit, I. Yulevich, E. Maguid, D. Ozeri, D. Veksler, V. Kleiner, and E. Hasman, Spin-optical metamaterial route to spin-controlled photonics, *Science* **340**, 724 (2013).
- [14] X. Ling, X. Zhou, X. Yi, W. Shu, Y. Liu, S. Chen, H. Luo, S. Wen, and D. Fan, Giant photonic spin Hall effect in momentum space in a structured metamaterial with spatially varying birefringence, *Light Sci. Appl.* **4**, e290 (2015).
- [15] B. Wang, E. Maguid, K. Rong, M. Yannai, V. Kleiner, and E. Hasman, Photonic topological spin Hall effect mediated by vortex pairs, *Phys. Rev. Lett.* **123**, 266101 (2019).
- [16] W. J. M Kort-Kamp, Topological phase transitions in the photonic spin Hall effect, *Phys. Rev. Lett.* **119**, 147401 (2017).
- [17] L. Cai, M. Liu, S. Chen, Y. Liu, W. Shu, H. Luo, and S. Wen, Quantized photonic spin Hall effect in graphene, *Phys. Rev. A* **95**, 013809 (2017).
- [18] W. Zhang, W. Wu, S. Chen, J. Zhang, X. Ling, W. Shu, H. Luo, and S. Wen, Photonic spin Hall effect on the surface of anisotropic two-dimensional atomic crystals, *Photon. Res.* **6**, 511 (2018).
- [19] W. Zhang, Y. Wang, S. Chen, S. Wen, and H. Luo, Photonic spin Hall effect in twisted few-layer anisotropic two-dimensional atomic crystals, *Phys. Rev. A* **105**, 043507 (2022).
- [20] A. Aiello, N. Lindlein, C. Marquardt, and G. Leuchs, Transverse angular momentum and geometric spin Hall effect of light, *Phys. Rev. Lett.* **103**, 100401 (2009).
- [21] A. Aiello, P. Banzer, M. Neugebauer, and G. Leuchs, From transverse angular momentum to photonic wheels, *Nat. Photon.* **9**, 789 (2015).
- [22] L.-J. Kong, S.-X. Qian, Z.-C. Ren, X.-L. Wang, and H.-T. Wang, Effects of orbital angular momentum on the geometric spin Hall effect of light, *Phys. Rev. A* **85**, 035804 (2012).
- [23] M. Neugebauer, T. Bauer, S. Orlov, N. Lindlein, A. Aiello, and G. Leuchs, Geometric spin Hall effect of light in tightly focused polarization-tailored light beams, *Phys. Rev. A* **89**, 013840 (2014).
- [24] J. Korger, A. Aiello, V. Chille, P. Banzer, C. Wittmann, N. Lindlein, C. Marquardt, and G. Leuchs, Observation of the geometric spin Hall effect of light, *Phys. Rev. Lett.* **112**, 113902 (2014).
- [25] S. He, J. Zhou, S. Chen, W. Shu, H. Luo, and S. Wen, Spatial differential operation and edge detection based on the geometric spin Hall effect of light, *Opt. Lett.* **45**, 877 (2020).
- [26] Y. Aharonov, D. Z. Albert, and L. Vaidman, How the result of a measurement of a component of the spin of a spin-1/2 particle can turn out to be 100, *Phys. Rev. Lett.* **60**, 1351 (1988).
- [27] J. Dressel, M. Malik, F. M. Miatto, A. N. Jordan, and R. W. Boyd, Colloquium: Understanding quantum weak values: Basics and applications, *Rev. Mod. Phys.* **86**, 307 (2014).
- [28] O. Hosten and P. Kwiat, Observation of the spin Hall effect of light via weak measurements, *Science* **319**, 787 (2008).
- [29] Y. Gorodetski, K. Y. Bliokh, B. Stein, C. Genet, N. Shitrit, V. Kleiner, E. Hasman, and T. W. Ebbesen, Weak measurements of light chirality with a plasmonic slit, *Phys. Rev. Lett.* **109**, 013901 (2012).
- [30] X. Zhou, X. Ling, H. Luo, and S. Wen, Identifying graphene layers via spin Hall effect of light, *Appl. Phys. Lett.* **101**, 251602 (2012).
- [31] S. Chen, X. Ling, W. Shu, H. Luo, and S. Wen, Precision measurement of the optical conductivity of atomically thin crystals via the photonic spin Hall effect, *Phys. Rev. Appl.* **13**, 014057 (2020).
- [32] T. Zhu, Y. Lou, Y. Zhou, J. Zhang, J. Huang, Y. Li, H. Luo, S. Wen, S. Zhu, Q. Gong, M. Qiu, and Z. Ruan, Generalized spatial differentiation from the spin Hall effect of light and its application in image processing of edge detection, *Phys. Rev. Appl.* **11**, 034043 (2019).
- [33] J. Zhou, H. Qian, C. F. Chen, J. Zhao, G. Li, Q. Wu, H. Luo, S. Wen, and Z. Liu, Optical edge detection based on high efficiency dielectric metasurface, *Proc. Natl. Acad. Sci. USA* **116**, 11137 (2019).
- [34] J. Liu, Q. Yang, S. Chen, Z. Xiao, S. Wen, and H. Luo, Intrinsic optical spatial differentiation enabled quantum dark-field microscopy, *Phys. Rev. Lett.* **128**, 193601 (2022).
- [35] J. Liu, Q. Yang, Y. Shou, S. Chen, W. Shu, G. Chen, S. Wen, and H. Luo, Metasurface-assisted quantum nonlocal weak-measurement microscopy, *Phys. Rev. Lett.* **132**, 043601 (2024).
- [36] R. Wang, S. He, and H. Luo, Photonic spin-Hall differential microscopy, *Phys. Rev. Appl.* **18**, 044016 (2022).
- [37] Y. Shou, J. Liu, and H. Luo, When optical microscopy meets all-optical analog computing: A brief review, *Front. Phys.* **18**, 42601 (2023).
- [38] D. Xu, W. Xu, Q. Yang, W. Zhang, S. Wen, and H. Luo, All-optical object identification and three-dimensional reconstruction based on optical computing metasurface, *Opto-Electron Adv.* **6**, 230120 (2023).
- [39] S. Liu, S. Chen, S. Wen, and H. Luo, Photonic spin Hall effect: Fundamentals and emergent applications, *Opto-Electronic Sci.* **1**, 220007 (2022).
- [40] J. D. Jackson, *Classical Electrodynamics* (Wiley, New York, 1999).
- [41] J. A. Stratton, *Electromagnetic Theory* (John Wiley and Sons, New York, 2007).
- [42] A. Aiello and M. Ornigotti, Near field of an oscillating electric dipole and cross-polarization of a collimated beam of light: Two sides of the same coin, *Am. J. Phys.* **82**, 860 (2014).
- [43] M. Ornigotti and A. Aiello, The Hertz vector revisited: A simple physical picture, *J. Opt.* **16**, 105705 (2014).
- [44] L. W. Davis, Theory of electromagnetic beams, *Phys. Rev. A* **19**, 1177 (1979).
- [45] J. Lekner, Polarization of tightly focused laser beams, *J. Opt. A: Pure Appl. Opt.* **5**, 6 (2003).
- [46] K. Y. Bliokh, E. A. Ostrovskaya, M. A. Alonso, O. G. Rodríguez-Herrera, D. Lara, and C. Dainty, Spin-to-orbital angular momentum conversion in focusing, scattering, and imaging systems, *Opt. Express* **19**, 26132 (2011).
- [47] Y. Fainman and J. Shamir, Polarization of nonplanar wave fronts, *Appl. Opt.* **23**, 3188 (1984).
- [48] A. Aiello, C. Marquardt, and G. Leuchs, Nonparaxial polarizers, *Opt. Lett.* **34**, 3160 (2009).
- [49] T. Wilson, R. Juskaitis, and P. Higdon, The imaging of dielectric point scatterers in conventional and confocal polarisation microscopes, *Opt. Commun.* **141**, 298 (1997).

- [50] D. Haefner, S. Sukhov, and A. Dogariu, Spin Hall effect of light in spherical geometry, *Phys. Rev. Lett.* **102**, 123903 (2009).
- [51] O. G. Rodríguez-Herrera, D. Lara, K. Y. Bliokh, E. A. Ostrovskaya, and C. Dainty, Optical nanoprobing via spin-orbit interaction of light, *Phys. Rev. Lett.* **104**, 253601 (2010).
- [52] J. S. Eismann, L. H. Nicholls, D. J. Roth, M. A. Alonso, P. Banzer, F. J. Rodríguez-Fortuño, A. V. Zayats, F. Nori, and K. Y. Bliokh, Transverse spinning of unpolarized light, *Nat. Photon.* **15**, 156 (2021).
- [53] D. Paul, D. K. Sharma, and G. V. Pavan Kumar, Focused linearly-polarized-light scattering from a silver nanowire: Experimental characterization of the optical spin-Hall effect, *Phys. Rev. A* **103**, 013520 (2021).
- [54] E. A. Essex, Hertz vector potentials of electromagnetic theory, *Am. J. Phys.* **45**, 1099 (1977).
- [55] P. Varga and P. Török, Exact and approximate solutions of Maxwell's equations for a confocal cavity, *Opt. Lett.* **21**, 1523 (1996).
- [56] T. Zhu, C. Guo, J. Huang, M. Orenstein, Z. Ruan, and S. Fan, Topological optical differentiator, *Nat. Commun.* **12**, 680 (2021).